JGR Oceans

RESEARCH ARTICLE
10.1029/2021JC018201

Towards Retrieving Reliable Ocean Surface Currents in the Coastal Zone From the Sentinel-1 Doppler Shift Observations

A. Moiseev[1], J. A. Johannessen[1,2], and H. Johnsen[3]

[1]Nansen Environmental and Remote Sensing Center, Bergen, Norway, [2]Geophysical Institute, University of Bergen, Bergen, Norway, [3]NORCE Norwegian Research Center AS, Tromsø, Norway

Key Points:

- The Sentinel-1 Doppler shift observations are used to retrieve information about the ocean surface currents in the coastal zone
- Mesoscale eddies are detected in the Synthetic Aperture Radar-derived ocean surface current radial velocity fields
- Combination of the wind and wave information from collocated models improves the accuracy of the wave-induced contribution estimates

Correspondence to:

A. Moiseev,
artem.moiseev@nersc.no

Citation:

Moiseev, A., Johannessen, J. A., & Johnsen, H. (2022). Towards retrieving reliable ocean surface currents in the coastal zone from the Sentinel-1 Doppler shift observations. *Journal of Geophysical Research: Oceans*, *127*, e2021JC018201. https://doi.org/10.1029/2021JC018201

Received 5 NOV 2021
Accepted 31 JAN 2022

Author Contributions:

Conceptualization: J. A. Johannessen
Supervision: J. A. Johannessen
Writing – review & editing: J. A. Johannessen

Abstract Recent developments on calibration and partitioning of the signal between the wave and current contributions significantly improve the accuracy of geophysical retrievals from Sentinel-1 Synthetic Aperture Radar-based Doppler shift measurements in the open ocean. In this study, we revise the Sentinel-1B Interferometric Wide products acquired from December 2017 to January 2018 along the coastal zone of northern Norway. We find that the satellite attitude is responsible for 30% of the variation in the Doppler shift observations, while the antenna pattern can describe an additional 15%. The residual variation after recalibration is about 3.8 Hz, corresponding to 0.21–0.15 m/s radial velocity (RVL) depending on the incidence angle. Using recalibrated Sentinel-1 observations, collocated with near-surface wind from MetCoOp-Ensemble Prediction System and sea state from MyWaveWAM, we develop an empirical function (CDOP3SiX) for estimating the sea-state-induced Doppler shift. CDOP3SiX improves the accuracy of sea state contribution estimates under mixed wind fetch conditions and demonstrates that the Norwegian Coastal Current can be detected in the Sentinel-1 derived ocean surface current RVL maps. Moreover, two anticyclonic mesoscale eddies with radial velocities of about 0.5 m/s are detected. The surface current patterns are consistent with the collocated sea surface temperature observations. The Doppler shift observations from Sentinel-1 can therefore be used to study ocean surface currents in the coastal zone with a 1.5 km spatial resolution.

Plain Language Summary Knowledge of ocean surface currents is crucial for studies of volume, heat and salt transport, tracking pollutants, and fisheries. The Doppler shift from Sentinel-1 Synthetic Aperture Radar (SAR) observations can be used to retrieve information about ocean surface currents. Challenging calibration and lack of algorithms for separating the wave and current contributions have limited the application of this observation-based method. Recent developments on calibration showed promising improvements in the accuracy of the signal. In this study, we apply this recent calibration method to Sentinel-1B scenes and develop an algorithm applicable for the challenging conditions in the coastal zone. We found that the signal from the Norwegian Coastal Current can be detected in the Sentinel-1 derived ocean surface current radial velocity fields. Also, we demonstrated the potential of SAR data for observing eddies with diameter of about 40–70 km. The Sentinel-1 derived surface currents express meandering structures and boundaries in consistence with the satellite-based sea surface temperature field. Comparison with the ocean model also reveals reasonable agreement, especially for the major surface current features. Therefore, given accurate calibration and new algorithm for removal of the wind and wave contribution, the Sentinel-1 observations can be used for monitoring ocean surface currents in the coastal zone with high spatial resolution.

1. Introduction

Coastal ocean currents are usually measured from in situ surface drifters (Haza et al., 2018; Röhrs & Christensen, 2015), fixed moorings, and land-based HF radars (Barrick et al., 1977). However, these measurements are irregular in time and space and/or cover only a limited area yielding observation gaps. The Doppler shift-based radial surface current retrievals from the Synthetic Aperture Radars (SARs) may be used to complement existing coastal observations, yielding more comprehensive and high-resolution mapping of the coastal ocean surface currents as shown by data from Envisat ASAR (Chapron et al., 2005; Hansen et al., 2011; Johannessen et al., 2008), TerraSAR/TanDEM-X (Romeiser et al., 2013), and Sentinel-1 A/B missions (Moiseev, Johnsen, Hansen, & Johannessen, 2020). The Sentinel-1 SAR is an operational constellation of two satellites (A and B) operated by the European Space Agency (ESA). The Sentinel-1 Interferometric Wide (IW) swaths are available up to two times a day in high-latitude coastal zones, depending on the region (ESA, 2017–2018). Previously, these data have shown promising results for retrieving Norwegian Coastal Current (NCC) features (Moiseev, Johnsen,

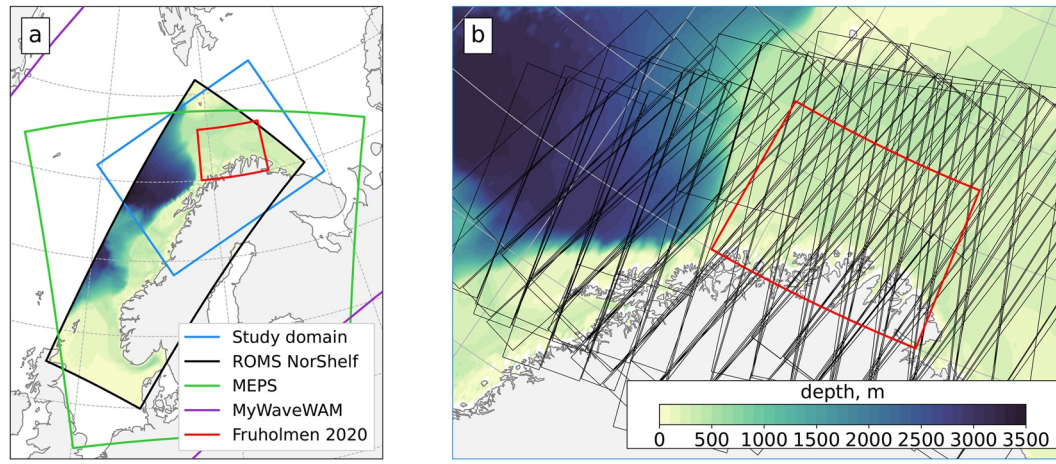

Figure 1. (a) Extent of the regional Regional Ocean Modeling System (ROMS) NorShelf, MetCoOp-Ensemble Prediction System (MEPS), and MyWaveWAM models used in the study. Blue contour indicates the domain of the study. (b) Detailed bathymetry map (color) of the region of study from the GEBCO data set. Black frames represent a footprint of Sentinel-1B Interferometric Wide scenes. Red rectangular box indicates the region from Moiseev, Johnsen, Hansen, and Johannessen (2020).

Hansen, & Johannessen, 2020). However, Moiseev, Johnsen, Hansen, and Johannessen (2020) also noted issues related to calibration and separation of the geophysical signal between the sea state and ocean surface current. Recent advances in the calibration technique based on the use of the gyroscope telemetry (OceanDataLab, 2019) considerably improved the accuracy of the geophysical retrievals from the Sentinel-1 Doppler shift measurements, as documented using Sentinel-1 WaVe (WV) mode observations over the global ocean (Moiseev, Johnsen, Johannessen, et al., 2020). Moreover, the refinement of an empirical Geophysical Model Function (GMF) based on these newly calibrated Doppler shift observations combined with near-surface wind and sea state information derived from respective numerical models yielded an improved estimate of the sea-state-induced contribution to the Doppler shift and in turn, more accurate retrievals of the open ocean surface currents.

Given these recent developments, it is therefore timely to revisit the Sentinel-1 IW data acquisitions for the coastal zone. The wave development in the deep water coastal zone can significantly differ from the open ocean due to fetch limitations affecting the signal detected by SAR. Besides, the IW swaths are acquired at a wider range of incidence angles compared to the WV vignettes, providing an opportunity to study the sensitivity of Doppler shift measurements to the wind/wave conditions under various SAR acquisition geometries. In this study, we use Sentinel-1B IW scenes collocated with regional operational numerical models to evaluate the high-resolution Doppler shift observations under various environmental conditions along the coast of northern Norway (Figure 1b). We further develop a GMF for predicting the sea-state-induced signal as a function of the wind, wind sea, and swell at the time of SAR acquisition considering a wide range of incidence angles. As in situ observations are not available for proper validation, we assess the potential of using Sentinel-1B IW ocean surface radial velocity retrievals for detecting mesoscale ocean surface current features in the coastal zone using available ocean model forecasts and satellite-derived Sea Surface Temperature (SST) fields.

2. Data and Methods

We used 144 independent Sentinel-1B Interferometric Wide (IW) Level 2 Ocean (OCN) scenes acquired from ascending and descending passes, VV polarization, over the Norwegian coastal zone (113 scenes) (Figure 1b), and the Amazon rainforest areas (31 scenes) from December 2017 to January 2018. Each scene is a composite of 3–5 consecutive frames acquired in Terrain Observation with Progressive Scans SAR (TOPSAR, De Zan & Guarnieri, 2006) mode. Each frame, in turn, consists of 3 subswaths with a total width of 250 km and incidence angles, θ, varying from 30.1° to 46.0°. Not all Sentinel-1 IW acquisitions are processed into the Level 2 products due to the limited capacities of the ESA Instrument Processing Facility (IPF). Therefore, we generated Level 2 OCN products from the available Level 0 RAW data (Copernicus, 2017–2018) by using (a) TOPSAR mode data processor (Engen & Larsen, 2011) to generate Level 1 Single Look Complex (SLC) products from the Level 0

Table 1
Data Sets Used in the Study

Data set	Resolution		Parameter [units]	Source	Data provider
	Spatial	Temporal			
Sentinel-1 IW Raw Data		–	I, Q components	Sentinel-1 IW Level 0 products	ESA
Ocean surface radial velocity	1.5 km	–	Doppler shift [Hz], Incidence angle [deg.], Platform heading [deg.]	Sentinel-1 IW Level 2 OCN products	Norce
Sentinel-1 attitude variation	–	2 s.	Row, pitch, and yaw angles [mdeg.]	Sentinel-1B gyroscope	Ocean DataLab/ESA
Near-surface wind field	2.5 km	1 hr	Wind speed at 10 m [m/s], Wind direction at 10 m [deg.]	MEPS	MET Norway
Wind sea and Swell field	4 km	1 hr	Significant wave height [m], Mean wave period [sec.], Mean wave direction [deg.]	MyWaveWam	MET Norway
Ocean surface current	2.4 km	1 hr	Surface current speed [m/s], Surface current direction [deg.]	ROMS NorShelf model forecast	MET Norway
Bathymetry	15 arc. sec	–	Bathymetric height [m]	GEBCO	BODC

RAW data and (b) Sentinel-1 Level 2 processor (Engen & Johnsen, 2011) to generate the Level 2 OCN RVL products from the Level 1 SLC. Despite the implementation of the processor is different from the standard ESA IPF routine, the final Level 2 data are expected to be similar to the original products provided by Copernicus. To achieve a better signal-to-noise ratio, we resampled Level 2 OCN products on the grid with a 1.5 × 1.5 km cell size.

These Sentinel-1B IW scenes are collocated with regional operational numerical models for the near-surface wind field, ocean waves, and ocean surface current as shown in Table 1. Detailed bathymetry of the study area is derived from GEBCO.

2.1. Sentinel-1 IW Doppler Shift Observations

Data acquired over rainforests are routinely used to evaluate the SAR observations as they provide uniform scattering areas yielding stable signals in the backscatter as shown by the Doppler shift profiles extracted from Sentinel-1B IW Level 2 products in Figure 2. In general, the Doppler shift estimates are composed of several contributing sources (OceanDataLab, 2019) as expressed by:

$$f_{dc} = f_{bias}(\beta) + f_{att}(\beta, \theta_{att}(t)) + f_{sca} + \underbrace{(f_{osc} + f_{ss})}_{f_{rvl}} + \Delta f \quad (1)$$

where:

1. f_{bias} is the antenna electronic miss-pointing term related to the gradual degradation of the SAR antenna and the consequent change of the antenna beam pattern yielding deviation from the nominal pointing. This term has a distinct pattern within each subswath in the range (across-track) direction yielding "jumps" in the signal between subswaths (Figure 2a). In the azimuth (along-track) direction, the bias is stable within an orbit
2. f_{att} is the miss-pointing error due to satellite attitude roll, pitch, and yaw deviations, θ_{att}, from the nominal steering at time t. This signal is rapidly changing in the azimuth direction (for example, Figures 2b) and is a function of the boresight angle β in the range direction
3. f_{sca} is the scalloping error due to SAR antenna sweep motion in the TOPSAR acquisition mode (Figure 2c) related to the elevation direction antenna element pattern (AEP) envelope that weighs the total phased array beam pattern yielding bias in the beam center
4. f_{rvl} is the geophysical signal related to the ocean surface radial velocity (RVL) that can be approximated as a sum of the sea-state-induced motion (so-called wave bias), f_{ss}, and the underlying ocean surface current, f_{osc}. Hence, it is zero over land. Over the ocean, on the other hand, $f_{rvl} > 0$ / $f_{rvl} < 0$ represents surface motion toward/away from the SAR antenna

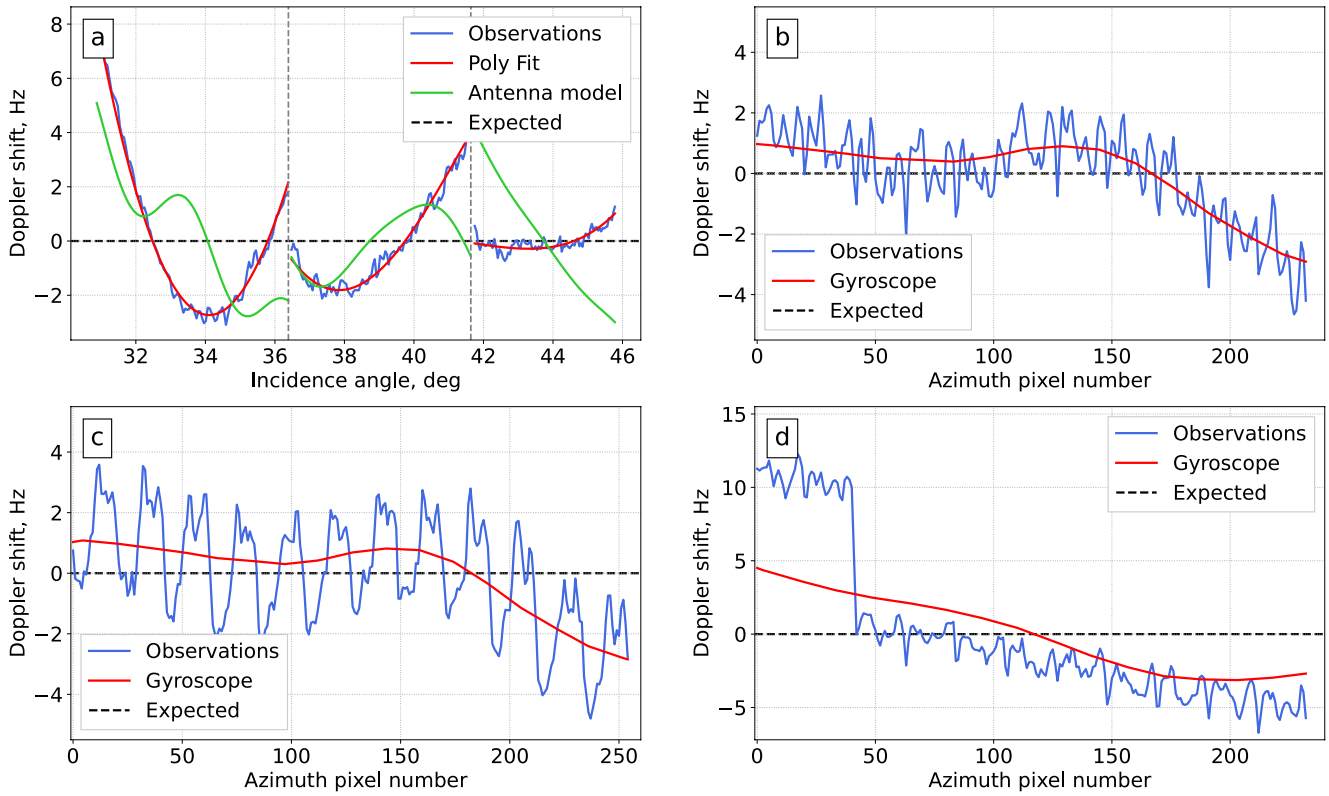

Figure 2. Doppler shift profiles extracted from Sentinel-1B Interferometric Wide (IW) scene acquired over the rainforest area on 28 December 2017 at 23:11.19: (a) Mean range (across-track) Doppler shift profile from observations (blue) and antenna model (green); (b and c) Mean azimuth (along-track) Doppler shift profile from observations (blue) and Doppler error due to attitude variation estimated from the gyroscope telemetry (red) for the second and first subswath, respectively. (d) Mean azimuth Doppler shift profile from observations (blue) and Doppler error due to attitude variation estimated from the gyroscope telemetry (red) for the second subswath from the Sentinel-1B IW scene acquired over the rainforest area on 31 December 2017 at 21:58.50.

5. Δf is the total residual error related to the inaccurate calibration, periodical automatic compensation of the temperature-dependent gain, and phase variations of the transmit and receive modules of the Sentinel-1 SAR instrument (e.g., Figure 2d) and other unknown biases

The range (Figure 2a) and azimuth (Figure 2b) f_{dc} profiles from the Sentinel-1B IW scene acquired on 28 December 2017 at 23:11.19 over the rainforest area show that the f_{bias} computed from the antenna model (e.g., Figure 2a green) and f_{att} (e.g., Figure 2b blue) estimated from the down-linked quaternions in the Sentinel-1 Level 2 processor do not correctly represent non-geophysical Doppler shift variations in the data (Johnsen et al., 2016).

Assuming that f_{bias} and f_{att} do not change within a scene, the non-zero f_{dc} acquired over the land (within the scene) can be used to approximate and remove these contributions from observations acquired over the ocean within the same scene (Hansen et al., 2011; Johnsen et al., 2016). However, although f_{bias} is typically stable over several orbits, f_{att} is rapidly changing within the same scene (e.g., Figure 2b blue). The novel approach outlined by OceanDataLab (2019) employs telemetry from the gyroscope operating onboard the satellite to determine its deviation from the nominal attitude and hence the estimate of f_{att}. Figure 2b shows good agreement between tendency in the observed f_{dc} (Figure 2b blue) and the f_{att} (Figure 2b red) estimated from gyroscope data. After removal of the f_{att}, the residual f_{bias}, associated with the antenna electronic miss-pointing, can be approximated (Figure 2a red) using observations acquired over the land (Figure 2a blue) on a scene-by-scene basis.

Capitalizing on an analysis of 2.1×10^6 pixels from 31 independent Sentinel-1B IW scenes acquired over rain forests, we found that, on average, about 30% of the standard deviation in the Doppler shift observations, σ_{dc}, can be associated with the satellite attitude variation (Table 2). An additional 15% of the σ_{dc} is related to the SAR *antenna electronic miss-pointing*. The residual σ_{dc} in recalibrated data is 3.8 Hz, corresponding to 0.21–0.15 m/s ground-range radial velocity depending on θ. Comparison with the traditional calibration technique (i.e., without

Table 2
Descriptive Statistics for the Doppler Shift Observations Acquired by Sentinel-1B Interferometric Wide From December 2017 to January 2018 Over the Rainforest Areas

Processing step	Mean	Median	Std
Measured Doppler shift	26.553	26.536	6.903
Attitude corrected Doppler shift	26.797	26.534	4.824
Antenna pattern corrected Doppler shift	0.0	−0.116	3.823
Classic data-driven calibration (No prior attitude information)	0.0	−0.116	4.051

any prior attitude information) does not reveal a significant difference on a global scale. However, the value of attitude information is evident on a scene-by-scene basis (e.g., Figure 2b).

Several issues with f_{dc} observations from Sentinel-1 are yet to be properly explored. First, the periodic variation in the azimuth direction with an amplitude of about 4 Hz (e.g., Figure 2c blue) is especially notable in the first subswath. Although some calibration techniques are outlined in the literature (e.g., Elyouncha et al., 2019), the systematic application is yet to be evaluated. Second, the jumps in f_{dc} are in the azimuth direction with a magnitude of about 10 Hz (Figure 2d). These jumps can be associated with periodical automatic compensation of the temperature-dependent gain and phase variations of the transmit and receive modules of the Sentinel-1 SAR instrument. This will alter the nominal antenna excitation coefficients and thus also the overall antenna gain pattern, and subsequently also the estimated Doppler shift. This phenomenon can be visually identified within a scene due to its large magnitude. In this study, we, therefore, rely on the visual inspection for removing SAR scenes with these erroneous f_{dc} retrievals. Essentially, we demonstrated that the availability of prior attitude information increases the precision of the f_{dc} signal in IW data, which, in turn, should improve the quality of the geophysical retrievals.

2.2. Near-Surface Wind, Sea State, and Ocean Surface Current Information From Models

Wind field: The regional MetCoOp-Ensemble Prediction System (MEPS) provides hourly forecasts of the wind field at 10 m height with 2.5 km horizontal resolution, and more than half of its domain is representing the open ocean (see Figure 1a). The model is forced by the ECMWF-IFS and assimilates measurements of surface temperature, snow cover, moisture fields, and various upper-air observations, etc. (For more details see Müller et al. (2017)). From validation against in-situ observations, MEPS provides more accurate temperature and wind forecasts compared to the ECMWF-IFS, especially in areas of complex coastal topography. We therefore collocated available SAR data with wind speed, u_{10}, and direction, ϕ, at 10 m height from openly available model forecasts (MET Norway, 2017–2018) on a scene-by-scene basis (Figure 3a). In doing so, the direction ϕ was reprojected with respect to the SAR antenna look direction such as 0° and 180° direction represents upwind and downwind while 90° and 270° represent along-track winds.

Sea state: The regional MyWave WAM model provides openly available hourly forecasts of the sea state on a 4-km horizontal grid covering both European seas and the Arctic Ocean (Figure 1a). The model is forced with winds from the ECMWF and AROME (for details on the model setup see Saetra (2016). Following (Moiseev, Johnsen, Johannessen, et al., 2020), we describe the sea state at the time of SAR acquisition using mean wave period, T_m, mean wave propagation direction, ψ_m, and significant wave height, H_s, extracted from the model forecasts (MET Norway, 2017–2018). Thanks to the wave partitioning available in the MyWave products, we use T_m^w, ψ_m^w, and H_s^w separately for the wind sea (Figures 3b and 3c) and the swell (Figures 3d and 3e), where w either indicates the wind sea (ws) or the swell (sw). The swell is further characterized by two phenomena, notably (a) Remotely generated swell independent from the local wind field and (b) Locally generated swell, that is, waves generated within the domain and marked as the swell in the model when the wind of a particular direction drops to 0 m/s. Thus, we consider averaged information about the ensemble of wind waves and swell corresponding to mean wave energy at the time of SAR acquisition. Following wind preprocessing, ψ_m^w were projected with respect to the SAR antenna look direction. Following Yurovsky et al. (2019), we used $u_{ovl} = \omega_m^w H_s$ as a metric for wave orbital velocity, where $\omega_m^w = 1/T_m^w$ is the wave frequency in Hz.

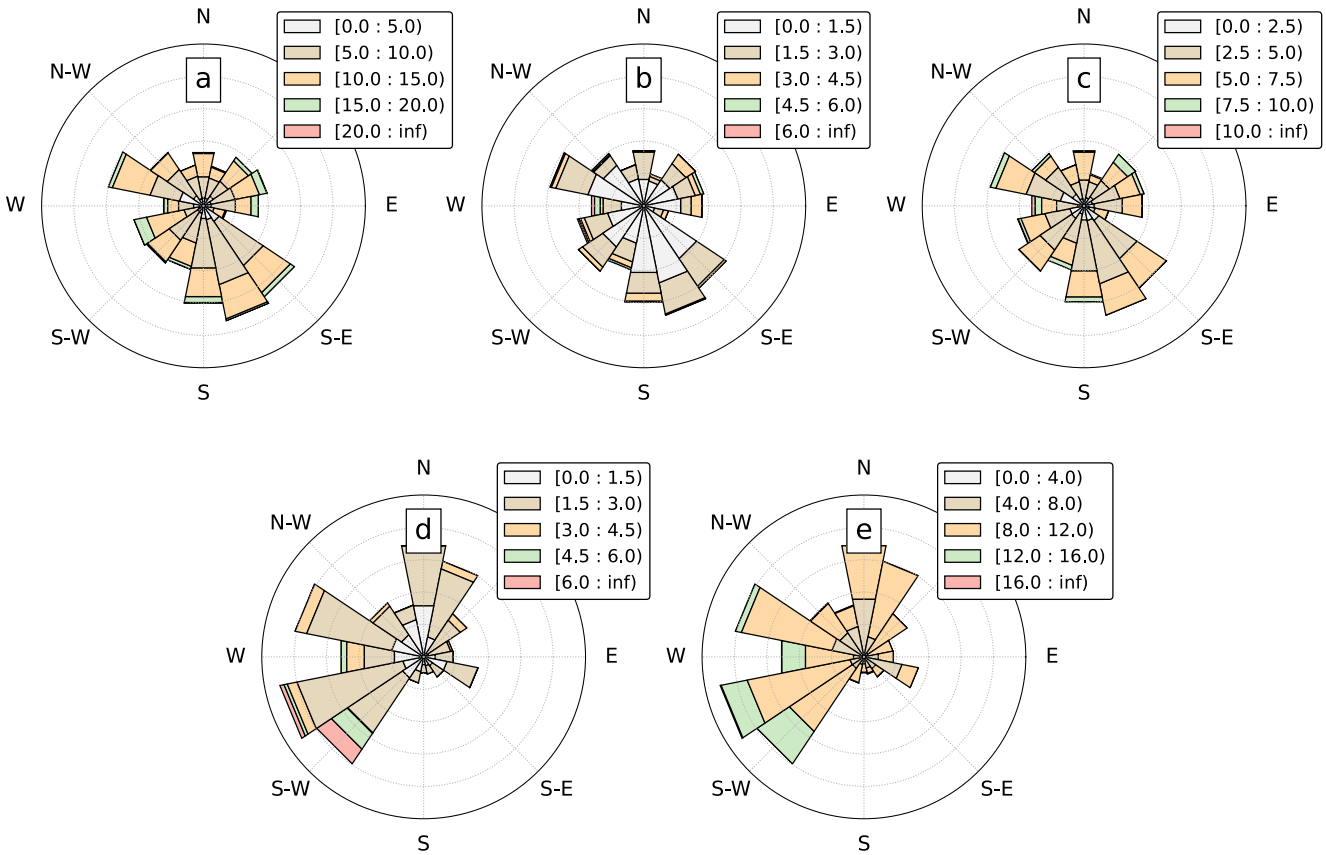

Figure 3. Directional distribution of (a) wind speed and 10 m height in m/s, (b) mean wind sea significant wave height in m, (c) mean wind sea period in s, (d) swell significant wave height in m, and (e) swell period in s.

Surface Currents: The high-resolution Regional Ocean Modelling System (ROMS) NorShelf provides an hourly forecast of the ocean surface current velocity (corresponding to the 0.2–1.2 m depth) on a 2.4 km horizontal grid covering the Norwegian coastal zone (Figure 1a). The NorShelf is forced by the atmospheric fields from ECMWF. More details on the model setup are available from (Röhrs et al., 2018).

Precise collocation of all data sets was implemented using the GeoSPaaS framework and Nansat software (Korosov et al., 2016). Thanks to the hourly availability of all model forecasts, the time difference between the SAR acquisitions, and the model field did not exceed 30 min. Based on the collocated wind/wave data from the respective model simulations, we studied f_{rvl} as a function of a wide range of the wind/wave conditions (Figure 3) using simple regression analysis.

2.3. Data Selection and Training of the Geophysical Model Function (GMF)

The representativeness of a training data set constrains the accuracy of an empirical Geophysical Model Function (GMF). Hence, it is crucial to select SAR acquisitions where the observed ocean surface motion is primarily induced by the sea state. The wave-current interactions have a significant impact on the sea state (Ardhuin et al., 2017; Kudryavtsev et al., 2017). Although Moiseev, Johnsen, Hansen, and Johannessen (2020) found a qualitative agreement between ROMS forecast and SAR observations in a position of the NCC, retrieving the reliable f_{osc} from each model grid cell is still a challenge. Therefore, we rely on the accurate position of the main surface current features in the model forecast for masking SAR pixels where the model simulated surface current velocity was bigger than 0.20 m/s (47% of the data set). As we attempt to focus on deep water conditions, 3% of the observations, where the bottom depth was smaller than half of the wavelength (from the model), were discarded. Considering the influence of coastal orography on the wind field we also removed grid cells acquired closer than 20 km from the coast (14% of the data set).

About 4.15×10^6 collocated pixels representing a wide range of environmental conditions (Figure 3) were available after selection. Assuming the absence of the signal from the surface current in the data set, we used simple linear regression analysis to establish relationships between the Doppler shift observations and range components of the near-surface wind speed, as well as wind sea, and swell orbital velocities for a range of incidence angles. Finally, we used this data set to train an empirical GMF for predicting sea-state-induced Doppler shift for a given wind field, sea state, and radar configuration. The GMF, based on an Artificial Neural Network (ANN) approach, was compiled, thanks to the openly available Python Tensorflow software. The performance of the model was compared to the CDOP model (Mouche et al., 2012) based on randomly subselected testing data.

2.4. Sea Surface Temperature From MODIS-Aqua

We collocated 8-day averaged night Sea Surface Temperature (SST) products from the MODIS-Aqua (NASA Goddard Space Flight Center, 2018) with available Sentinel-1B data on the scene-by-scene basis. Collocation to single snapshots was unfortunately not available due to frequent cloud cover. However, 8-day averages for the SST field are sufficient for qualitative comparison to the structures or patterns in the SAR Doppler-based radial velocity retrievals.

3. Results

3.1. Sentinel-1 Doppler Shift Observations in the Coastal Zone Under Different Environmental Conditions

We evaluated the SAR-derived ground-range ocean surface radial velocities, u_{rvl}, as a function of the near-surface wind and sea state, considering onshore and offshore wind directions. In the absence of surface currents, the u_{rvl} is related to the sea-state-induced motion in the SAR antenna range direction. In the first order, the u_{rvl} can be approximated as a function of the range-directed wind speed at 10 m height (x_{10}) (Chapron et al., 2005; Moiseev, Johnsen, Johannessen, et al., 2020). As expected, the Sentinel-1 u_{rvl} retrievals strongly correlate ($r \approx 0.86$) with x_{10} (Figure 4a). We estimated that the u_{rvl} is about 10% of x_{10} at $\theta \approx 36°$ under onshore wind directions. This estimate is consistent with 12% previously estimated for the global open ocean from Sentinel-1 WV observations and ECMWF winds (see Figure 3f from Moiseev, Johnsen, Johannessen, et al., 2020), assuming that the wind sea development in the (deep water) coastal zone under onshore wind is similar to the open ocean. The difference in the linear regression slope can be related to (a) undersampling of wind regimes in the regional compared to the global data set, (b) different sensitivity of IW and WV data to the wind features due to spatial resolution of utilized L2 products (1.5 km for IW (this study) and 20 km for WV Moiseev, Johnsen, Johannessen, et al. (2020)), and (c) errors in the ECMWF and MEPS wind fields. When the wind blows offshore, the correlation between u_{rvl} and x_{10} is considerably weaker ($r \approx 0.76$). Although most observations were acquired with $u_{10} < 11$ m/s, under stronger offshore winds the u_{rvl} grows at a slower rate (Figure 4d) compared to onshore winds (Figure 4a). We relate it to the underdeveloped wind sea since the fetch required for the fully developed seas (FDS) under winds over 7 m/s is rapidly exceeding 100 km (with over 500 km for 15 m/s), which is not achievable for the winds blowing offshore in the coastal zone.

We further take advantage of the IW swath data to extend the analysis for a broader range of incidence angles between $\theta \approx 31°$ (near-range) and $\theta \approx 46°$ (far-range). Analysis of the linear regression slopes between the u_{rvl} and x_{10} suggests dependency on the incidence angle (Table 3). The u_{rvl} decreases from a maximum of 12% of x_{10} at $\theta \approx 31°$ to 7% at $\theta \approx 46°$. The slow-moving Bragg wave contributions increase with the incidence angle, yielding a decrease in the u_{rvl} (Collard et al., 2008; Johannessen et al., 2008; Mouche et al., 2008). Although on average, the x_{10} provides a simple proxy for the sea state at the time of SAR acquisition, this approach does not account for wind fetch and history and swell waves.

The fetch limitations affect the wind wave development yielding underdeveloped seas and hence, different from the FDS signal captured by SAR. Thanks to the wave partitioning available in the collocated model forecasts, we study the u_{rvl} as a function of the range-directed wind wave, x_{ws}, and the swell, x_{sw}, orbital velocities. We represented u_{rvl} as a function of x_{ws} at $\theta \approx 36°$ for onshore (Figure 4b) and offshore (Figure 4e) wind conditions. The x_{ws} provides a better approximation for the u_{rvl} than x_{10} (Figures 4a and 4d) as fewer outliers are detected in

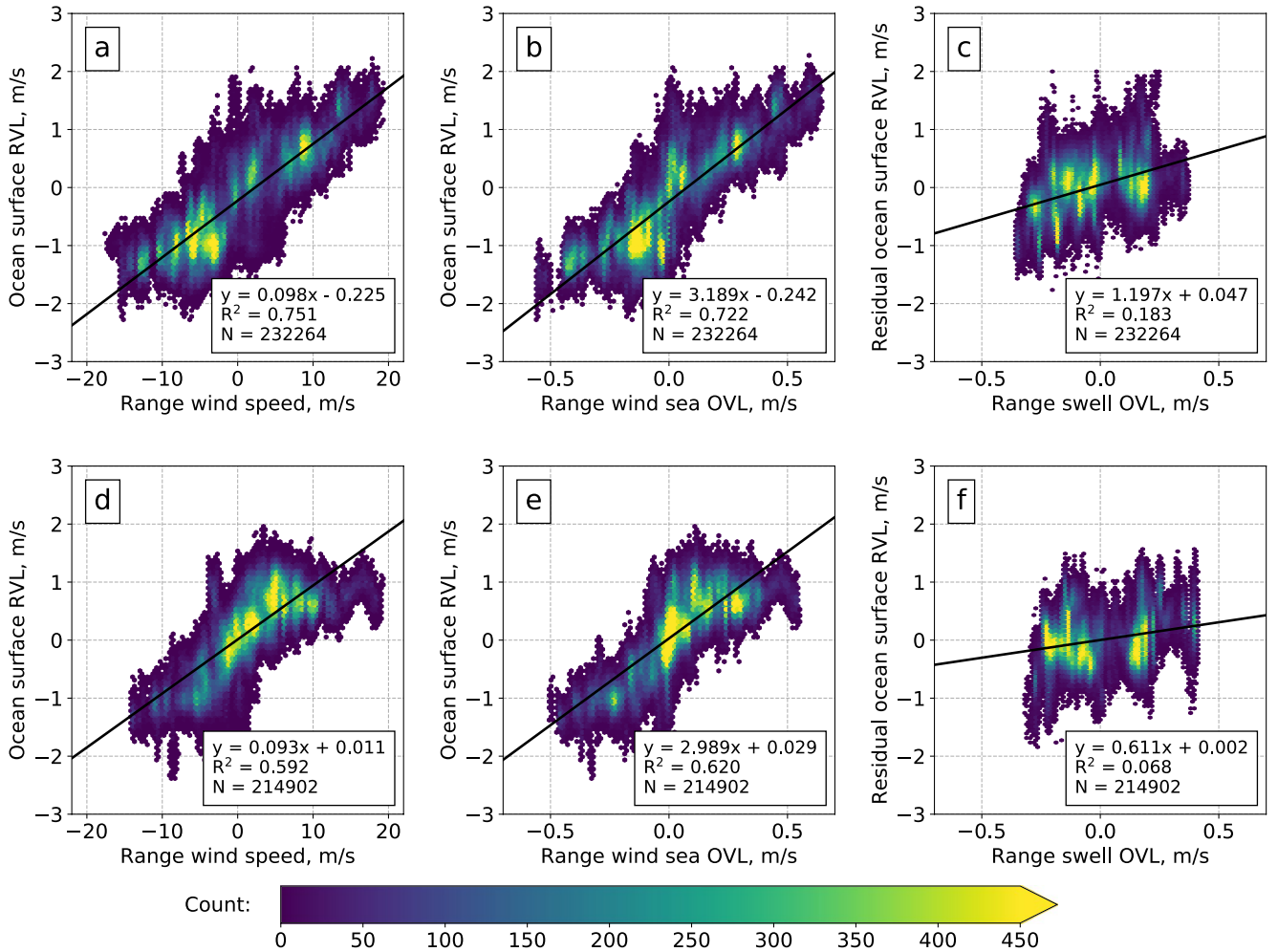

Figure 4. The ocean surface radial velocity (RVL) derived from Sentinel-1B Interferometric Wide products acquired at 36° incidence angle in onshore (top) and offshore (bottom) wind conditions as a function of the near-surface wind speed (a and d) and wind sea orbital velocity (b and e) projected of the Synthetic Aperture Radar (SAR) range direction. Panels (c and f) represent the residual RVL, after removal of the wind sea induced motion, as a function of the swell orbital velocity projected of the SAR range direction. The color scale represents the number of observations. The black line and corresponding equation (right bottom corner) represent linear regression.

the relationship especially at lower sea states. The model-derived wind sea, based on averaged information from the wind waves ensemble accounts for the history and fetches, delivering a more accurate representation of the wind sea at SAR acquisition time than the FDS.

Table 3
Linear Regression Between the Ocean Surface Radial Velocity From Sentinel-1 Interferometric Wide and the Near-Surface Wind Speed in the Range Direction From Interferometric Wide for Onshore Wind Cases Estimated for a Range of Incidence Angle Bins

Incidence	31.0–33.5	33.5–36.0	36.0–38.5	38.5–41.0	41.0–43.5	43.5–46.0
N	285422	302195	290703	300299	262556	200045
LRS	0.123	0.106	0.091	0.084	0.079	0.074
LRI	−0.28	−0.22	−0.21	−0.15	−0.09	−0.07
R^2	0.79	0.75	0.76	0.76	0.77	0.88

Note. LRS and LRI indicate linear regression slope and intercept, respectively.

Assuming no background surface currents, the motion of the facets detected by SAR is induced by the joint modulation from the wind waves and swell. Given that the available data were acquired under virtually constant presence of the swell (Figures 3d and 3e), its contribution to the signal must be evaluated. To estimate the impact of the swell-induced motion on the recorded u_{rvl}, we, first, used the linear regression model (Table 3) to remove the wind sea contribution from the observations. In general, we observe a weak relationship between the residual u_{rvl} and x_{sw}. The low correlation can be related to (a) residual wind sea signal in the observations and (b) errors in wave partitioning in the model. Notably, with increasing incidence angle, the swell contribution becomes completely neglectable. Nevertheless, following Yurovsky et al. (2019), we assume that it is necessary to consider the impact of swell

Table 4
List of Empirical Geophysical Model Functions (GMFs) for Estimation of the Sea State Contribution to the Synthetic Aperture Radar C-Band Doppler Shift Observations

			Geophysical model function			
Parameter		Notation	CDOP[a]	CDOP3S[b]	CDOP3SX[c]	CDOP3SiX[c]
Wind	Speed	u_{10}	x	x		
	Direction	ϕ	x	x		
	Range speed	x_{10}			x	x
Wave	Significant height	H_s		x		
	Mean period	T_m		x		
	Mean direction	ψ_m		x		
	Mean ROVL[d]	x_{total}			x	
	Wind Sea ROVL	x_{ws}				x
	Swell ROVL	x_{sw}				x
SAR	Incidence	θ	x	x	x	x
	Polarization	p	x	x	x	x
Training data specification						
SAR platform			Envisat ASAR	Sentinel-1B	Sentinel-1B	Sentinel-1[e]
SAR acquisition mode			WSM	WV	WV	IW
SAR incidence angle			15° – 45°	23° & 36°	23° & 36°	30° – 46°
Wind source			ECMWF	ECMWF	ECMWF	MEPS
Wave source			–	WW3	WW3	MyWaveWAM
Pixel size[f]			8 × 3.5 km	20 × 20 km	20 × 20 km	1.5 × 1.5 km
Training domain			Global	Global	Global	Coastal

Note. The upper part specifies wind/wave/SAR parameters (x-marked) used for approximation of the sea-state-induced Doppler shift in the respective GMF. The lower part specifies the data set used for fitting the respective GMF. Note, that wind/wave directions are represented with respect to SAR antenna look direction.

[a]For details on data set and training see Mouche et al., 2012. [b]For details on data set and training see Moiseev, Johnsen, Johannessen, et al., 2020. [c]Developed in this paper. [d]ROVL–Range-directed orbital velocity. [e]Data set is used in this paper for the cross-evaluation of all available GMFs. [f]Pixel size is the size of a grid cell utilized in the collocated data set and can be different from the original wind/wave/SAR products.

on a case-by-case basis especially for low wind speeds or along-track wind directions when the signal detected by SAR is dominated by swells.

3.2. Geophysical Model Function (GMF) for Estimation of the Sea-State-Induced Contributions to the C-Band Doppler Shift Observations

Several empirical GMFs for predicting f_{ss} have been developed for Envisat ASAR (Collard et al., 2008; Mouche et al., 2012) and the presently operational Sentinel-1B WV (Moiseev, Johnsen, Johannessen, et al., 2020) C-band SAR Doppler shift observations (see Table 4). The performances of these GMFs have been further intercompared and assessed in the new simulation experiments discussed below using Sentinel-1B IW high-resolution coastal data set.

Assuming that f_{ss} is only due to locally generated wind waves, f_{ww}, Mouche et al. (2012) developed an empirical GMF for predicting the wind-wave-induced contribution to the C-band Doppler shift observations (*CDOP*), based on the Envisat ASAR data collocated with wind from the ECMWF:

$$f_{ss} \approx f_{ww} = CDOP\,(u_{10},\ \phi,\ \theta,\ p) \tag{2}$$

where u_{10} is the wind speed at 10 m height, ϕ is the wind direction with respect to SAR antenna look direction, θ is the incidence angle, and p indicates the SAR polarization. Using Sentinel-1B WV data acquired in the open ocean, on the other hand, Moiseev, Johnsen, Johannessen, et al. (2020) found that *CDOP* systematically underestimates f_{ss} by about 25%. Moreover, simulations for 0–12 m/s winds at $\theta = 36°$ and $\theta = 43°$ reveal that: (a) $f_{ss} \neq 0$ Hz for $u_{10} = 0$ m/s and (b) $|f_{ss}|$ decreases with ϕ from about 130° to 180° (downwind) at $\theta = 43°$ for all u_{10} (Figure 5a). In addition, when compared with Sentinel-1B IW observations in the coastal zone, the *CDOP* underestimates f_{ss} by about 18% and 30%, respectively, for onshore/offshore winds (Figure 5b/5c) at $\theta \approx 36°$. The *CDOP* does not account for any direct sea state information and therefore relies on the fully developed sea (FDS) assumption for the corresponding wind field. However, in the coastal zone, the FDS assumption is unlikely for offshore wind yielding poorer results for those cases.

Applying the Sentinel-1B WV observations acquired in the global open ocean, Moiseev, Johnsen, Johannessen, et al. (2020) developed a GMF called *CDOP3S* that accounts for the mean wave field (i.e., combined wind sea and swell) in addition to the wind field:

$$f_{ss} = CDOP3S\,(u_{10},\ \phi,\ H_s,\ T_m,\ \psi_m,\ \theta,\ p) \tag{3}$$

where H_s is the significant wave height, T_m is the mean wave period, and ψ_m is the mean wave propagation direction derived from WAVEWATCHIII (WW3) with respect to SAR antenna look direction. However, the simulation in *CDOP3S* (Figure 5d, dashed lines) does not reproduce the realistic f_{ss} suggesting an overfit of the empirical GMF during training.

In this paper, an updated model function *CDOP3SX* is therefore proposed, in which:

$$f_{ss} = CDOP3SX\,(x_{10},\ x_{\text{total}}, \theta,\ p) \tag{4}$$

where $x_{10} = -u_{10}cos\phi$ is the range-directed component of the wind vector at 10 m. In general, the sea-state-induced signal detected by SAR is related to the facet orbital motion (Chapron et al., 2005). Hence, we also substituted the H_s, T_m, and ψ_m with the range-directed component of the wave orbital velocity $x_{total} = -(H_s/T_m)cos\psi_m$. As such, by accounting for the combined wind- and wave-induced motion *CDOP3SX* seems to reproduce more realistic f_{ss} function (Figure 5d, solid lines). Moreover, *CDOP3SX* yields the largest values for $|f_{ss}(\phi = 180°)|$ while $f_{ss}(u_{10} = 0) \approx 1Hz$, which is closer to the expected $f_{ss}(u_{10} = 0) = 0Hz$ (in the absence of swell) compared to the *CDOP* (Figure 5a). The bias of about 1 Hz at $u_{10} = 0$ m/s and $\phi = 90°$ is likely related to the: (a) Errors in the wind/wave direction that has a strong impact around $\phi \approx 90°$ and (b) residual non-geophysical signal due to calibration errors. Note that for the simulation we considered $x_{total} = 0.3x_{10}$ following the estimate from Moiseev, Johnsen, Johannessen, et al. (2020) that is consistent with the FDS assumption. Therefore, as the SAR is sensitive only to the line-of-sight ocean surface motion, we found that the combined use of the x_{10} and x_{total} yields better generalization in the model compared to previously used directional wind and wave fields (e.g., Moiseev, Johnsen, Johannessen, et al., 2020; Mouche et al., 2012).

While *CDOP3SX* applies Sentinel-1B IW coastal observations at $\theta \approx 36°$, on the other hand, it shows a significantly bigger spread compared to the *CDOP* although it captures the general tendency. The bigger spread can be related to the: (a) Differences in the sea state fields in the open ocean (training) and the coastal zone (testing) and (b) differences in the corresponding wave models used for training (WW3) and testing (MyWave). Moreover, the *CDOP3SX* model cannot reproduce the difference between the onshore/offshore wind cases (Figure 5e/5f) suggesting that the global mean wave field is not sufficient for approximating underdeveloped seas in the coastal zone. In addition, the *CDOP3SX* is constrained to $\theta = 36°$ that also limits its application for the IW data acquired for $30.1° < \theta < 46°$.

The sea state at the time of SAR acquisition can be defined by several wave systems (e.g., wind sea and swell). Building on the advances of *CDOP3SX*, we replaced x_{total} with mean range wind sea (x_{ws}) and swell (x_{sw}) orbital velocities from MyWave to account for the mixed sea state conditions constrained by two different wave systems in the coastal zone. Based on the coastal data set (Section 2), we trained a new GMF called *CDOP3SiX* considering a wide range of θ:

$$f_{ss} = CDOP3SiX\,(x_{10},\ x_{\text{ws}},\ x_{\text{sw}}, \theta,\ p) \tag{5}$$

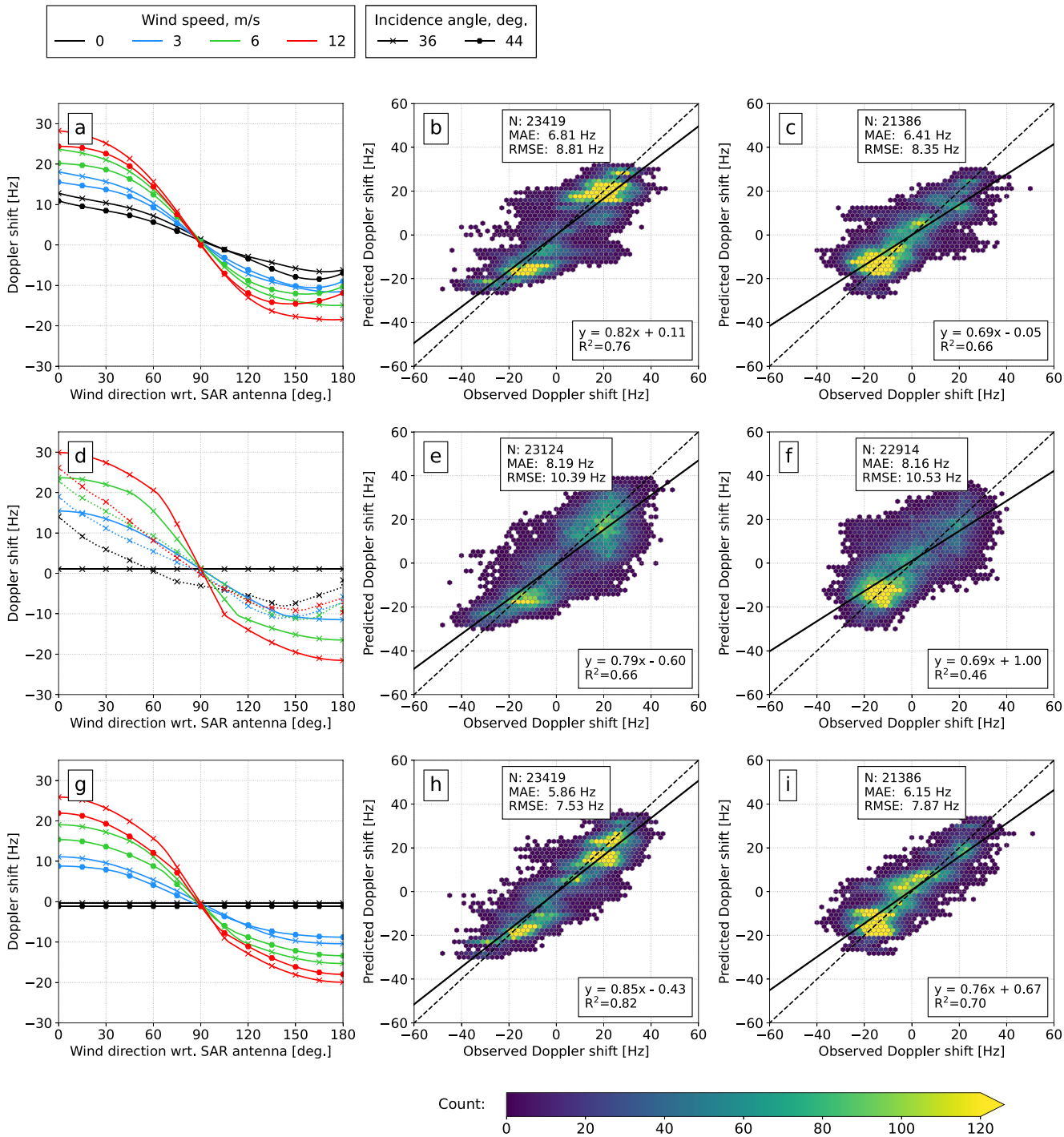

Figure 5. The evaluation of the sea-state-induced Doppler shift predicted using different empirical geophysical model functions (GMFs): CDOP (top row), CDOP3SX (middle row), and CDOP3SiX (bottom row). The left column shows the Doppler shift simulated using each respective model for the different wind speeds (color) and wind directions between 0° (downwind) and 180° (upwind) at two incidence angles 36° (x-markers) and 44° (o-markers). Note that since the $f_{ss}(\phi)$ is symmetric around $\phi = 180°$, we focus at $0° < \phi < 180°$. The dashed line in panel d represents CDOP3S model from Moiseev, Johnsen, Johannessen, et al. (2020). The middle and right columns represent comparison of the Doppler shift predicted by each respective GMF with Sentinel-1 Interferometric Wide Synthetic Aperture Radar observations at 36° incidence angle in onshore and offshore wind conditions, respectively. Mean Absolute Error (MAE), Root Mean Squared Error (RMSE), and number of observations (N) for each comparison are provided in the top center of each plot. Black line and inverter equation (right bottom corner) represent linear regression between observed and predicted Doppler shift.

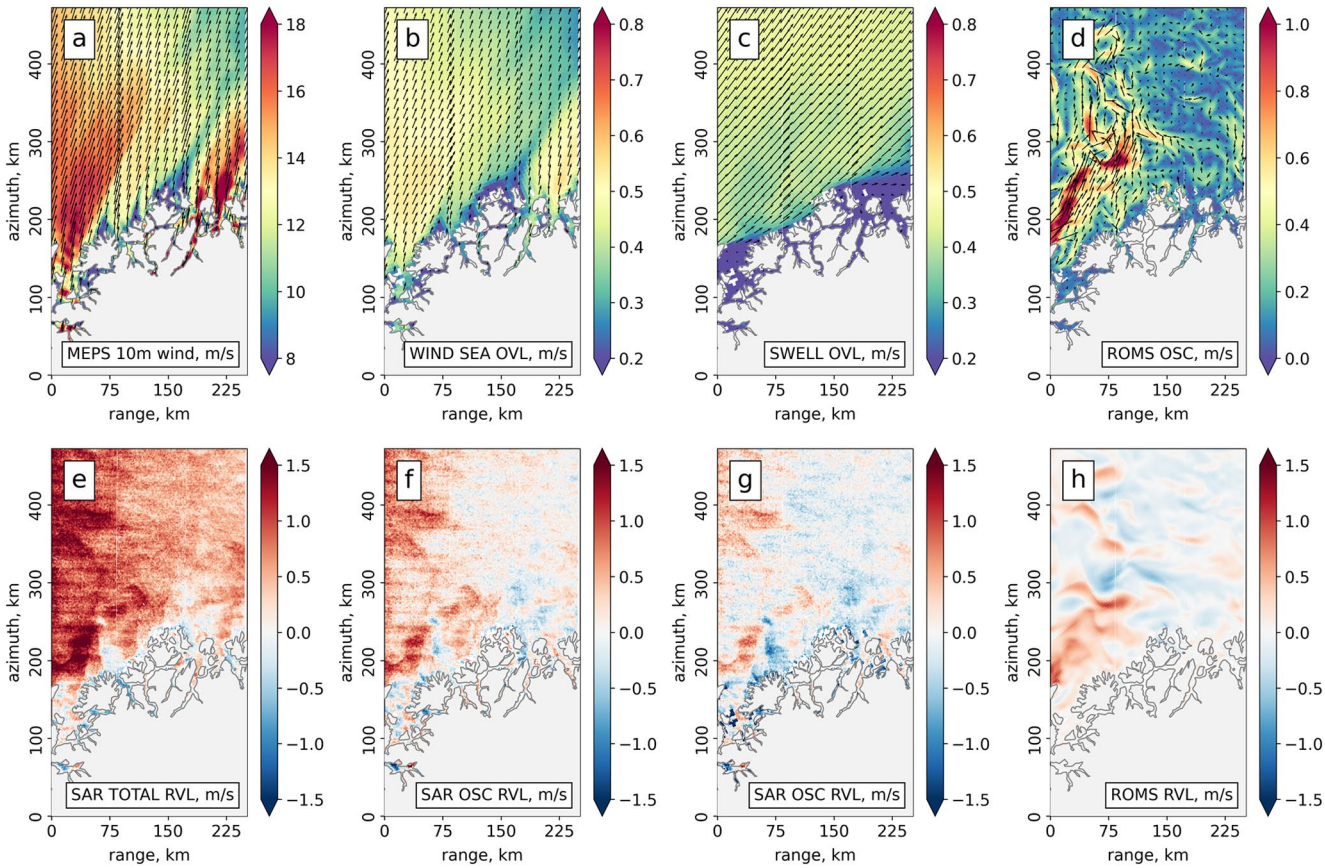

Figure 6. Ascending Sentinel-1B Interferometric Wide (IW) VV scene acquired in IW mode on 15 January 2018 at 16:06:06. The top row represents environmental conditions at the time of acquisition based on collocated model simulations (from the nearest hour if not specified): (a) Wind field at 10m height from MEPS in m/s; (b) wind sea mean orbital velocity from MyWave in m/s; (c) swell mean orbital velocity from MyWave in m/s; (d) Ocean surface current velocity on 15 January 2018 at 16:00:00 from Regional Ocean Modeling System (ROMS) NorShelf in m/s. The bottom row represents total ocean surface radial velocity (RVL) from the Sentinel-1B Doppler shift. (e) Ocean surface current RVL after removing wave-induced contribution estimated with (f) CDOP; (g) CDOP3SiX; and (h) Radial component of the surface current from the ROMS model in m/s. The positive/negative RVLs indicate motion to the east-northeast (right) and west-southwest (left).

Based on the simulation results (Figure 5g), we found that the *CDOP3SiX* reproduces the expected $f_{ss} \approx 0$ Hz for: (a) All u_{10} at $\phi = 90°$ and (b) $u_{10} = 0$ m/s at all ϕ. Note that for the simulation, we consider $x_{ws} = 0.3x_{10}$ and $x_{sw} = 0$ m/s that is consistent with the developed wind sea in the absence of the swell. The *CDOP3SiX* predicts f_{ss} that is up to 8(3) Hz lower for the 3(12) m/s downwind and up to 2(0.5) Hz higher for 3(12) m/s upwind compared with the *CDOP*. When compared with observations (Figures 5h and 5i), the *CDOP3SiX* shows smaller RMSE (by 1 Hz) and higher R^2 with the observations than the *CDOP*. However, despite overall improvements, we still found the difference in the signal predicted for the onshore (Figure 5h) and offshore (Figure 5i) wind cases that must be addressed in future development.

Although all GMFs summarized in Table 4 are based on observations from C-band SAR instruments, some inconsistencies in assessment may occur due to differences in acquisition mode, spatial resolution, and calibration.

3.3. Comparison of the Ocean Surface Current Retrievals

Figure 6 shows the Sentinel-1B IW scene acquired on 15 January 2018 at 16:06:06 in ascending pass over the northern coastal area of Norway. The scene was acquired under offshore winds ranging from 10 to 19 m/s (Figure 6a), yielding wind wave heights of 2–3.5 m with corresponding orbital velocities of 0.25–0.65 m/s (Figure 6b). A strong swell of 350–400 m length with up to 6–7 m height propagates north-eastward with corresponding orbital velocities of up to 0.5 m/s (Figure 6c). Note that this swell field is likely generated by a storm

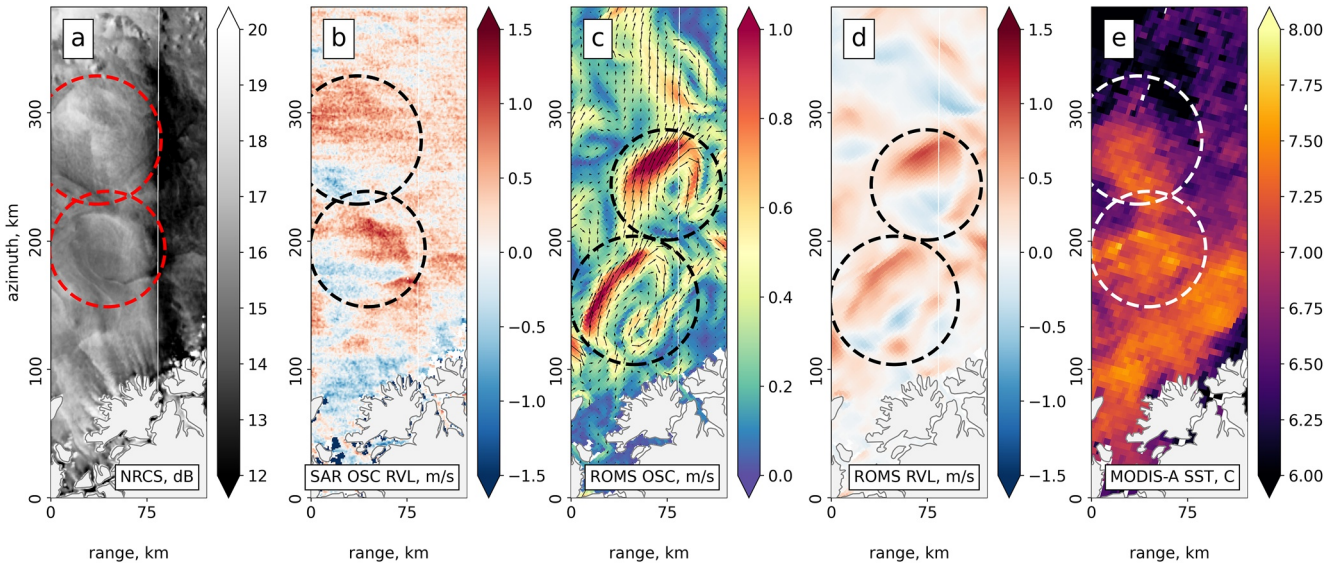

Figure 7. Ascending Sentinel-1B Interferometric Wide (IW) VV scene acquired in IW mode on 10 December 2017 at 16:06:07: (a) Normalized Radar Cross Section in dB; (b) Ocean surface current radial velocity (RVL) derived from the Doppler observations using CDOP3SiX model; (c) ocean surface current velocity from Regional Ocean Modeling System (ROMS) model at 16:00; (d) radial component of the ocean surface current RVL from the ROMS model; and (e) night-time sea surface temperature from MODIS-Aqua averaged between third and 10 December 2017. The positive/negative radial velocities ocean surface current to the right/left. The dashed circles indicate the areas of eddies detected in the subplot (a).

passing through the Norwegian sea around the time of acquisition. From this imaging geometry, the northeastward wind and wave motion corresponds to the ocean surface motion away from the antenna look direction yielding $u_{rvl} > 0$ (Figure 6e).

We retrieved the signal from the ocean surface current $f_{osc} = f_{rvl} - f_{ss}^{gmf}$ using different available GMFs for estimating f_{ss}. The f_{osc} retrievals were then converted to the ground range ocean surface current radial velocity, u_{osc}. The u_{osc} retrieved using the CDOP (Figure 6f) show a notable residual signal, especially in the near range, where the wave contribution is most significant. These residuals might be related to an impact of offshore propagating wind waves combined with the presence of extreme swell propagating along the coast. Despite residual f_{ss}, the Norwegian Coastal Current (NCC) flowing east-northeastward along the coast can be detected in the gradient of the f_{osc} field. However, the GMFs based only on the wind information do not provide reliable estimates of the f_{ss}, which in turn, reduces the accuracy of RVL retrievals.

By applying CDOP3SiX these impacts can be further quantified and removed as shown in Figure 6g. The NCC feature is now clearly detectable in the SAR derived u_{osc} field. Moreover, the structure of the NCC qualitatively agrees with the surface current radial velocity field derived from the regional ROMS NorShelf model (Figure 6h). Moreover, it is also likely that the residual signal in the open ocean near-range part of the scene can be related to the possible errors in the wind/wave model fields. All in all, based on this qualitative evaluation the CDOP3SiX provides more realistic estimates of the sea-state-induced contributions to the Doppler signal. In turn, improved retrievals of the surface current radial velocity in the coastal zone are derived.

3.4. Mesoscale Eddies in SAR Derived Ocean Surface Radial Velocity Field

Figure 7a shows the radar backscatter from the ascending Sentinel-1 IW scene acquired on 10 December 2017 at 16:06:07 (over the same area as shown in Figure 6). This image was obtained under moderate offshore winds ranging from 6 to 8.5 m/s, yielding wind waves of up to 1m height. In addition, a westward propagating swell field at 1–2.5 m heights was encountered. The backscatter pattern reveals the existence of two mesoscale eddies in near range. In consistence with this the CDOP3Si-based u_{osc} retrievals (Figure 7b) document the presence of both structures with $u_{osc} > 0$ and $u_{osc} < 0$ aligned nearby in azimuth direction suggesting evidence of two mesoscale anticyclonic eddies with radial velocities of 0.5 m/s. Furthermore, the simulated ocean surface current velocity

field (Figures 7c and 7e) is also revealing the presence of two anticyclonic eddies, although they are slightly misplaced compared with the observations. Finally, the two warm cores with sea surface temperatures of about 7°C detected in the nighttime MODIS-Aqua acquisitions between third and 10 December 2017 (Figure 7d) are also supporting this Sentinel-1B Doppler-based detection of the two anticyclonic eddies.

4. Conclusions

Recent developments in the calibration (OceanDataLab, 2019) and geophysical signal processing and separation (Moiseev, Johnsen, Johannessen, et al., 2020) have significantly improved the accuracy of the surface current radial velocity retrievals from the Sentinel-1 Doppler shift observations. In this study, we take advantage of these new developments to further improve the accuracy of the ocean surface current retrievals from the Sentinel-1B IW acquisitions in the challenging environmental conditions of the Norwegian coastal zone based on two months of observations in December 2017–January 2018.

We found that the unstable satellite attitude is responsible for about 30% of the variation in the Doppler shift observations, while antenna electronic miss-pointing can describe an additional 15%. After recalibration, the standard deviation in the Doppler shift observations over land is 3.8 Hz, corresponding to 0.15–0.21 m/s radial velocity depending on the incidence angle. This is a clear improvement compared to the 6.89 Hz previously reported by Moiseev, Johnsen, Hansen, and Johannessen (2020). However, artifacts related to the scalloping and antenna temperature compensation are still observed in the data set and must be addressed in future work.

We developed a new GMF called *CDOP3SiX* for predicting sea-state-induced contribution to the geophysical signal as a function of the range-directed components of wind speed from MEPS and wind sea and swell orbital velocities from MyWaveWAM model. The simulation experiment and application to the Sentinel-1B IW observations showed that the *CDOP3SiX* improves the accuracy of sea state contribution estimates due to addition of the wind sea and swell information compared to the previous *CDOP* model that relies only on the wind field. However, despite improvement, the *CDOP3SiX* still underperforms under offshore winds when the coastal orography and fetch limitation yields underdeveloped seas.

Given this new and accurate calibration and partitioning of the geophysical signal, the Sentinel-1B IW RVL estimates show promising capability to quantify meandering features and eddies within the Norwegian Coastal Current with a radial velocity of 0.5 m/s. These SAR Doppler-based surface current features are comparable with the surface current magnitudes and pattern derived from regional model simulations, although the simulations are partly misplacing some features. Moreover, the mesoscale structures derived from the satellite-based Sea Surface Temperature (SST) fields are also found to agree with the features derived from the Doppler shift.

Despite the study is constrained by only 2 months of observations from the single Sentinel-1B satellite, the results are promising. However, the limited number of SAR acquisitons is not sufficient for the robust validation, due to lack of in situ surface current observations in the area. Reprocessing of the full Sentinel-1 A/B data set using novel attitude calibration is therefore essential for further improvement of the empirical algorithms and validation. Moreover, the difference in wind/wave models used in the training and application due to the temporal-spatial distribution of the data sets can affect the performance of a GMF when applied to a particular data set (e.g., Sentinel-1 IW). Therefore, the next generation of GMF might explore the possibility to retrieve wind (see Dagestad et al., 2012) and wave (e.g., Nouguier, et al., 2018; Stopa et al., 2015) fields directly from the SAR observations, thus avoiding the use of numerical model fields that cannot realistically represent the high spatial variability in the wind and wave conditions that are typical for given SAR acquisitions. In turn, a highly valuable data set of Doppler-based radial velocities would stimulate more advanced studies of the upper ocean dynamics and comparison to numerical ocean model simulations and predictions, and eventually, assimilation of the SAR derived surface current retrievals.

Data Availability Statement

The full collocated dataset (including re-calibrated Sentinel-1 observations) is published in an open access repository (https://doi.pangaea.de/10.1594/PANGAEA.943627).

Acknowledgments
This work was performed under NERSC—251348/F50 and CIRFA 970422528 projects funded by the Norwegian Research Council. We would also like to thank ESA-ESRIN Sentinel 1 RVL Assessment Project and the Copernicus program for providing open access to the Sentinel-1B IW L2 OCN products. We are moreover grateful to the OceanDataLab for providing access to the Sentinel-1 attitude information and the Norwegian Meteorological Institute (MET Norway) for providing access to wind, wave, and current forecasts from the MEPS, MyWaveWAM, and ROMS NorShelf models openly distributed via the MET Norway Thredds server (https://thredds.met.no/, thredds.met.no/, CC 4.0 BY license).

References

Ardhuin, F., Gille, S. T., Menemenlis, D., Rocha, C. B., Rascle, N., Chapron, B., et al. (2017). Small-scale open ocean currents have large effects on wind wave heights. *Journal of Geophysical Research: Oceans*, *122*(6), 4500–4517. https://doi.org/10.1002/2016JC012413

Barrick, D. E., Evans, M., & Weber, B. (1977). Ocean surface currents mapped by radar. *Science*, *198*(4313), 138–144. http://www.jstor.org/stable/1744926

Chapron, B., Collard, F., & Ardhuin, F. (2005). Direct measurements of ocean surface velocity from space: Interpretation and validation. *Journal of Geophysical Research*, *110*(C7), C07008. https://doi.org/10.1029/2004JC002809

Collard, F., Mouche, A., Chapron, B., Danilo, C., & Johannessen, J. (2008). Routine high resolution observation of selected major surface currents from space. *Proceedings of SEASAR*, Frascati.

Copernicus (2017-2018). *Sentinel-1 data*. eu. Retrieved February 1, 2020, from scihub.copernicus.

Dagestad, K.-F., Horstmann, J., Mouche, A., Perrie, W., Shen, H., & Zhang, B. (2012). Wind retrieval from synthetic aperture radar-an overview. *4th SAR Oceanography Workshop (SEASAR 2012)* (pp. 18–22). ESA.

De Zan, F., & Guarnieri, A. M. (2006). TOPSAR: Terrain observation by progressive scans. *IEEE Transactions on Geoscience and Remote Sensing*, *44*(9), 2352–2360. https://doi.org/10.1109/TGRS.2006.873853

Elyouncha, A., Eriksson, L., Johnsen, H., & Ulander, L. (2019). *Using Sentinel-1 ocean data for mapping sea surface currents along the southern Norwegian coast. IGARSS 2019 - 2019 IEEE International Geoscience and Remote sensing Symposium* (pp. 8058–8061). IEEE. https://doi.org/10.1109/IGARSS.2019.8898468

Engen, G., & Johnsen, H. (2011). *Sentinel-1 Doppler and ocean radial velocity algorithm definition* (Vol. 59).

Engen, G., & Larsen, Y. (2011). Efficient full aperture processing of TOPS mode data using the moving band Chirp Z-Transform. *IEEE Transactions on Geoscience and Remote Sensing*, *49*(10), 3688–3693. https://doi.org/10.1109/TGRS.2011.2145384

ESA. (2017-2018). *Sentinel-1 observation Scenario*. (ESA) Retrieved January 2021, from Sentinel Online: Retrieved from https://sentinel.esa.int/web/sentinel/missions/sentinel-1/observation-scenario

Hansen, M. W., Collard, F., Dagestad, K.-F., Johannessen, J. A., Fabry, P., & Chapron, B. (2011). Retrieval of sea surface range velocities from envisat ASAR Doppler centroid measurements. *IEEE Transactions on Geoscience and Remote Sensing*, *49*(10), 3582–3592. https://doi.org/10.1109/TGRS.2011.2153864

Haza, A. C., D'Asaro, E., Chang, H., Chen, S., Curcic, M., Guigannd, C., et al. (2018). Drogue-loss detection for surface drifters during the Lagrangian Submesoscale Experiment (LASER). *Journal of Atmospheric and Oceanic Technology*, *35*(4), 705–725. https://doi.org/10.1175/JTECH-D-17-0143.1

Johannessen, J. A., Chapron, B., Collard, F., Kudryavtsev, V., Mouche, A., Akimov, D., & Dagestad, F. F. (2008). Direct ocean surface velocity measurements from space: Improved quantitative interpretation of Envisat ASAR observations. *Geophysical Research Letters*, *35*(22), 1–6. https://doi.org/10.1029/2008GL035709

Johnsen, H., Nilsen, V., Engen, G., Mouche, A. A., & Collard, F. (2016). Ocean Doppler anomaly and ocean surface current from Sentinel-1 TOPS mode. *International Geoscience and Remote sensing Symposium (IGARSS)* (pp. 3993–3996). IEEE. https://doi.org/10.1109/IGARSS.2016.7730038

Korosov, A., Hansen, M. W., Dagestad, K.-F., Yamakawa, A., Vines, A., & Riechert, M. (2016). Nansat: A Scientist-Orientated Python Package for Geospatial data processing. *Journal of Open Research Software*, *4*(1), 39. https://doi.org/10.5334/jors.120

Kudryavtsev, V., Yurovskaya, M., Chapron, B., Collard, F., & Donlon, C. (2017). Sun glitter imagery of surface waves. Part 2: Waves transformation on ocean currents. *Journal of Geophysical Research: Oceans*, *122*(2), 1384–1399. https://doi.org/10.1002/2016JC012426

MET Norway. (2017–2018). MEPS Archive. (MET Norway) Retrieved Feb 1, 2020, from MET Norway Thredds Service: Retrieved from https://thredds.met.no/thredds/catalog/meps25epsarchive/catalog.html

Moiseev, A., Johnsen, H., Hansen, M. W., & Johannessen, J. A. (2020). Evaluation of radial ocean surface currents derived from Sentinel-1 IW Doppler shift using coastal radar and Lagrangian surface drifter observations. *Journal of Geophysical Research: Oceans*, *125*(4). https://doi.org/10.1029/2019JC015743

Moiseev, A., Johnsen, H., Johannessen, J. A., Collard, F., & Guitton, G. (2020). On removal of sea state contribution to Sentinel-1 Doppler shift for retrieving Reliable Ocean surface current. *Journal of Geophysical Research: Oceans*, *125*(9). https://doi.org/10.1029/2020JC016288

Mouche, A., Chapron, B., Reul, N., & Collard, F. (2008). Predicted Doppler shifts induced by ocean surface wave displacements using asymptotic electromagnetic wave scattering theories. *Waves in Random and Complex Media*, *12*(1), 185–196. https://doi.org/10.1080/17455030701564644

Mouche, A., Collard, F., Chapron, B., Dagestad, K.-F., Guitton, G., Johannessen, J., et al. (2012). On the use of Doppler shift for sea surface wind retrieval from SAR. *IEEE Transactions on Geoscience and Remote Sensing*, *50*(7), 2901–2909. https://doi.org/10.1109/TGRS.2011.2174998

Müller, M. B., Batrak, Y., Kristiansen, J., Koltzow, M. A. O., Noer, G., & Korosov, A. (2017). Characteristics of a convective-scale weather forecasting system for the European Arctic. *Monthly Weather Review*, *145*(12), 4771–4787. https://doi.org/10.1175/MWR-D-17-0194.1

NASA Goddard Space Flight Center. (2018). *Sea-viewing wide field-of-view sensor (SeaWiFS) ocean color data, NASA OBDAAC/SEAWIFS/L2/OC/2018*. Ocean Ecology Laboratory, Ocean Biology Processing Group. https://doi.org/10.5067/ORBVIEW-2

Nouguier, F., Chapron, B., Collard, F., Mouche, A., Rascle, N., Ardhuin, F., & Wu, X. (2018). Sea surface kinematics from near-Nadir radar measurements. *IEEE Transactions on Geoscience and Remote Sensing*, *56*(10), 6169–6179. https://doi.org/10.1109/TGRS.2018.2833200

OceanDataLab (2019). *S-1 RVL DIL4: Algorithm description document*. ESRIN: ESA.

Röhrs, J., & Christensen, K. H. (2015). Drift in the uppermost part of the ocean. *Geophysical Research Letters*, *42*(23). https://doi.org/10.1002/2015GL066733

Röhrs, J., Sperrevik, A. K., & Christensen, K. H. (2018). *NorShelf: A reanalysis and data-assimilative forecast model for the Norwegian Shelf Sea*. Tech. Rep. ISSN 2387-4201 04/2018, Norwegian Meteorological Institute, https://doi.org/10.5281/zenodo.2384124.3.1.1

Romeiser, R., Runge, H., Suchandt, S., Kahle, R., Rossi, C., & Bell, P. S. (2013). Quality assessment of surface current fields from TerraSAR-X and TanDEM-X along-track interferometry and Doppler centroid analysis. *IEEE Transactions on Geoscience and Remote Sensing*, *52*(5), 2759–2772. https://doi.org/10.1109/TGRS.2013.2265659

Saetra, Ø. (2016). *MyWave project final report*. Norwegian Meteorological Institute.

Stopa, J., Ardhuin, F., Chapron, B., & Collard, F. (2015). Estimating wave orbital velocity through the azimuth cutoff from space-borne satellites. *Journal of Geophysical Research: Oceans*, *120*(11), 7616–7634. https://doi.org/10.1002/2015JC011275

Yurovsky, Y., Kudryavtsev, V., Grodsky, S., & Chapron, B. (2019). Sea surface Ka-band Doppler measurements: Analysis and model development. *Remote Sensing*, *411*(7), 839. https://doi.org/10.3390/rs11070839